JOURNAL OF MOLECULAR SPECTROSCOPY 92, 184–202 (1982)

Determination of the Electric Dipole Moment of the HSO Radical in Its $\tilde{X}^2A''(000)$ and $\tilde{A}^2A'(003)$ Electronic States

CHRISTOPHER R. WEBSTER,[1] PHILIP J. BRUCAT, AND RICHARD N. ZARE

Department of Chemistry, Stanford University, Stanford, California 94305

Stark shifts were measured for the zero-field-allowed 0_{00}–1_{10}, 1_{10}–0_{00} and zero-field-forbidden 0_{00}–1_{11}, 1_{11}–0_{00} lines of the HSO $\tilde{A}^2A'(003)$–$\tilde{X}^2A''(000)$ transition. A single-mode dye laser is used to record the Doppler-limited fluorescence excitation spectrum as a function of applied electric field (0–11 kV/cm) for excitation polarizations parallel and perpendicular to the applied field direction. The electric dipole moment along the *a* axis of this near-prolate asymmetric top is determined to be $\mu_a'' = 2.20 \pm 0.08$ D and $\mu_a' = 1.05 \pm 0.08$ D, in close agreement with recent ab initio calculations.

1. INTRODUCTION

The hydrosulfinyl radical, HSO, is the isovalent sulfur analog of the hydroperoxyl radical, HO_2, and as such, it plays an important role in the oxidation of sulfur-containing compounds. Becker *et al.* (*1, 2*) assigned a chemiluminescence spectrum in the range 520–960 nm to the $\tilde{A}^2A'$–$\tilde{X}^2A''$ transition in HSO, thereby providing the first spectroscopic evidence for the existence of this radical in the gas phase. More recently, Kakimoto *et al.* (*3*) excited fluorescence from the $\tilde{A}(003)$ vibronic state using a single-mode dye laser to record the first high-resolution spectrum of HSO. This Doppler-limited study led to the assignment of over 600 lines belonging to the $\tilde{A}(003)$–$\tilde{X}(000)$ band at 607 nm. These authors obtained accurate ground- and excited-state molecular constants, which made the present study possible. Endo *et al.* (*4*) were also able to record the microwave spectrum of HSO using a glow discharge cell, but because of the difficulty of obtaining a sufficient concentration of this short-lived reactive species in a Stark-modulated spectrometer, they were unable to measure the ground-state dipole moment.

Theoretical values of the $\tilde{A}$- and $\tilde{X}$-state dipole moments are available (*5, 6*). Sannigrahi *et al.* (*5*) calculated potential surfaces for these states using SCF and CI methods. They point out that the relative geometries of the $\tilde{A}$ and $\tilde{X}$ states are not consistent with qualitative MO theory. For this reason, experimental determination of the electric dipole moments of HSO in these two states is of special interest.

This paper reports the measurement of the electric dipole moment of HSO in both its $\tilde{A}(003)$ and $\tilde{X}(000)$ states. The laser-induced fluorescence excitation spectrum is obtained at Doppler-limited resolution for a series of static fields across

[1] Present address: Jet Propulsion Laboratory, California Institute of Technology, 4800 Oak Grove Drive, Pasadena, Calif. 91103.

0022-2852/82/030184-19$02.00/0

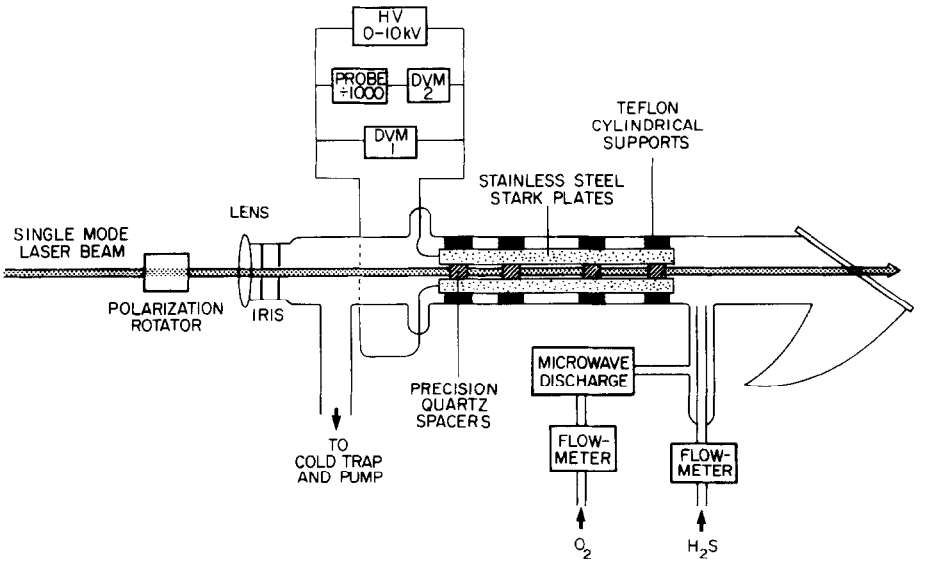

FIG. 1. Schematic of the Stark fluorescence cell. The fluorescence collection optics and photomultiplier tube are mounted at 90° to the plane of the figure.

Stark electrodes within the fluorescence cell. An actively-stabilized dye laser with a bandwidth nearly one thousand times narrower than the room temperature Doppler width ($\simeq$0.9 GHz) of HSO is used to measure the Stark shifts relative to the zero-field spectrum.

2. EXPERIMENTAL DETAILS

HSO is generated from the reaction of oxygen atoms with hydrogen sulfide in a fluorescence cell shown schematically in Fig. 1. High-purity O_2 (>99.9%) and H_2S (>99.5%) pass through flowmeters (Matheson 610) fitted with precision needle valves so that optimum conditions for radical production may easily be reproduced. All experiments reported here use 10 mTorr total cell pressure with an H_2S/O_2 partial pressure ratio of about 2/1. The gas flow rate at 10 mTorr is about 10 liters/sec. Oxygen atoms are produced by passing O_2 through a microwave discharge at 2450 MHz and 30 W power. The water-cooled discharge cavity (*7*) is located 30 cm upstream from the cell across a quartz tube fitted with a Wood's horn. The cell design ensures that the gas mixture flows through the center of the Stark electrodes before being pumped by a nitrogen cold trap.

A rhodamine 6G single-mode dye laser (Coherent 599-21) provides about 100 mW tunable output of $\simeq$1 MHz linewidth. The laser scan is monitored by a Fabry–Perot spectrum analyzer (Spectraphysics 470-01, 2 GHz FSR). A mechanical chopper interrupts the beam at 330 Hz and provides a reference for two lock-in amplifiers (PAR 124 A). The first lock-in records an I_2 fluorescence excitation spectrum for frequency calibration (*8*), and the second the HSO fluorescence excitation spectrum. These spectra are simultaneously stored in 2048 channels each of a signal averager (Nicolet 1170) triggered at the start of each scan. Typically, thirty 20-GHz scans are accumulated in 20 min using a 0.3-sec time constant on each lock-

in. Scan linearity and laser frequency drift are found to be $\simeq 1\%$ and <0.05 GHz, respectively, for the accumulation time used.

Before entering the cell the dye laser beam passes through a polarization rotator consisting of two Fresnel rhombs joined back to back. In combination with a linear polarizer, the beam polarization is then chosen to be either parallel or perpendicular to the electric field, thereby selecting $\Delta M_J = 0$ or $\Delta M_J = \pm 1$ transitions, respectively.

The Stark electrodes are stainless-steel plates, 100 mm long, 40 mm wide, and 4 mm thick, with screw-in electrical connections at one end. These plates are separated by eight precision quartz spacers of dimensions 4 mm square and 4.875 $\pm$ 0.005 mm thick (interferometrically measured). Four 10-mm-wide Teflon rings are pushed over the plates to firmly clamp them in place. A regulated high-voltage supply (Northeast Scientific) delivers 0–10 kV across the Stark plates. The field is determined in the following way: Two digital voltmeters (Keithley 179) calibrated to better than 0.05% are used. The first (DVM 1) is connected directly across the plates and the second (DVM 2) is connected in series with a $\div$ 1000 high-voltage probe (Tektronix P-6015). For a series of 10 voltages from 0 to 1 kV, readings on DVM 1 and DVM 2 are compared to calibrate the probe plus DVM 2 combination. The probe is determined to divide the plate voltage by a factor of 897 $\pm$ 2. Exchanging the two DVMs for each reading or removing DVM 1 from the circuit does not affect this result. For applied voltages greater than 1 kV, DVM 1 is disconnected from the circuit. Since the probe calibration factor shows no dependence on voltage from 0.001 to 1 kV and is specified to operate up to 20 kV, we use this calibration factor for applied voltages up to 6 kV, the highest reported in this experiment. The plate flatness, spacer thickness, and the probe and voltage calibration combine to give an error in the field across the plates of $\leq 1\%$. This error results in part because of the unavailability of a molecular calibration, such as a dipole moment determined with microwave accuracy. It should be noted that no problems are encountered with sulfur-containing solid deposition within the cell or inside the Stark plates. Indeed, at the low pressures (10 mTorr) used in this work, oxygen atom production appears to help keep the plates clean. Before a series of measurements, the plates, spacers, and rings are taken apart, boiled in dimethyl formamide (DMF), and cleaned in acetone before reassembly.

The fluorescence from HSO is weak, and the signal-to-noise ratio is optimized in the following manner: Scattered laser light is reduced by using a long-focal-length lens and irises to allow the beam to pass cleanly through the plates. A rotatable Brewster window reduces scattered light at the beam exit. The fluorescence is collected from a 10 mm $\times$ 1 mm region at the center of the Stark plates. The collection system comprises four cutoff filters (Corning 2-58) to reduce scattered laser light, two convex lenses, and an interference filter (Oriel 5443) located between the two lenses in a region of parallel light geometry. This filter transmits $\sim$10-nm band of light centered at 650 nm. The detection optics therefore isolate the HSO fluorescence emitted in the (003)–(001) band, whose peak intensity in the chemiluminescence spectrum of Schurath and co-workers (*2*) lies near 647 nm. The fluorescence signal from a photomultiplier tube (Hamamatsu R928) in a cooled housing (Products for Research TE-202) drives either a picoammeter (Keithley 427) or the lock-in amplifier.

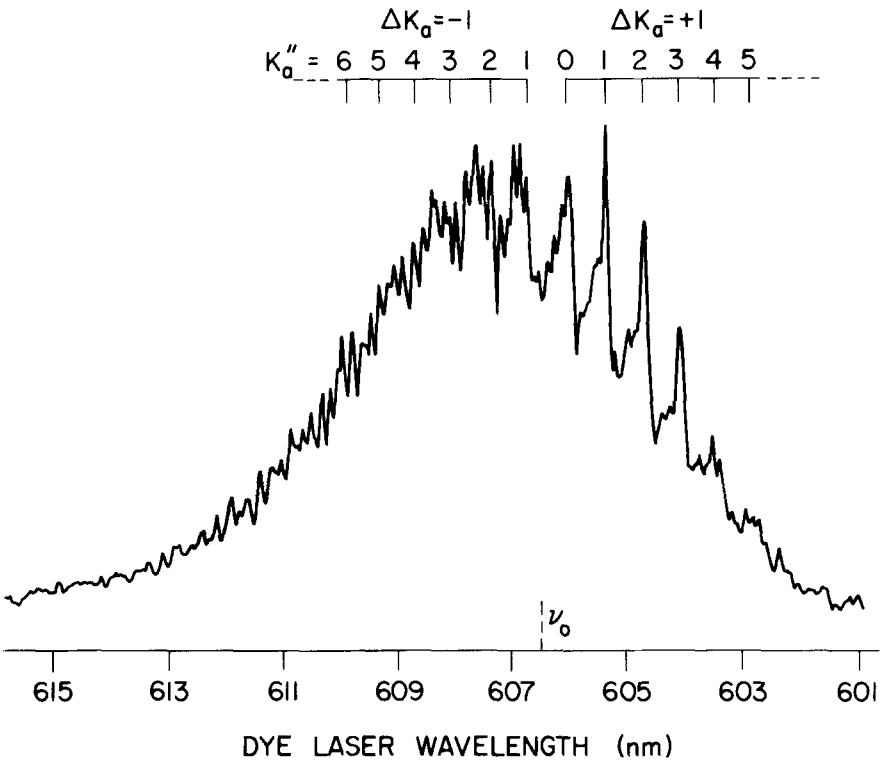

FIG. 2. The fluorescence excitation spectrum of the HSO $\tilde{A}(003)$-$\tilde{X}(000)$ band. K_a'' subband assignments are taken from Ref. (*3*).

The optical system is designed to discriminate strongly against light scattered from the laser, light from the microwave discharge, and non-HSO emitters. In a typical run the room lights, laser light, discharge light, and strong HSO fluorescence produce photomultiplier currents of 1.5×10^{-10}, 3.0×10^{-10}, 4.5×10^{-10}, and 3.6×10^{-9} A, respectively.

The best signal-to-noise ratio is found when the H_2S/O_2 ratio is just high enough to quench SO_2 emission and the total cell pressure is as low as possible. Introduction of the Stark electrode assembly, which lowers the pumping speed and increases available surface for wall reactions, reduces the HSO fluorescence signal by only a factor of 2.

3. OBSERVED SPECTRA

Figure 2 shows the fluorescence excitation spectrum of the $\tilde{A}(003)$-$\tilde{X}(000)$ band, recorded with the laser operating multimode (bandwidth $\simeq$ 10 GHz). This is a type-*c* band, the transition dipole lying perpendicular to the HSO plane. At shorter wavelengths, the ^RR K subband heads are clearly discernable, the subband head separation depending on a function $m(A'-B') - n(A''-B'')$ which remains approximately constant ($\simeq$18 cm^{-1}) over the observed region. The excitation spectrum is

virtually identical to the dispersed chemiluminescence (*2*). Both these spectra show the high density of rotational lines in this band, particularly near the band origin ν_0 where the weak 0_{00}–1_{10} and 1_{10}–0_{00} transitions are found.

High-resolution spectra demonstrating Stark shifts for perpendicular polarization are shown in Fig. 3. The zero-field $0_{00}(J = 1/2)$–$1_{10}(J = 1/2)$ F_2 component and $0_{00}(J = 1/2)$–$1_{10}(J = 3/2)$ F_1 component transitions near 16 472 cm^{-1} are readily identified from the line listings of Kakimoto *et al.* (*3*). Both these lines appear to tune with increasing electric field to lower frequency, losing intensity in the process.

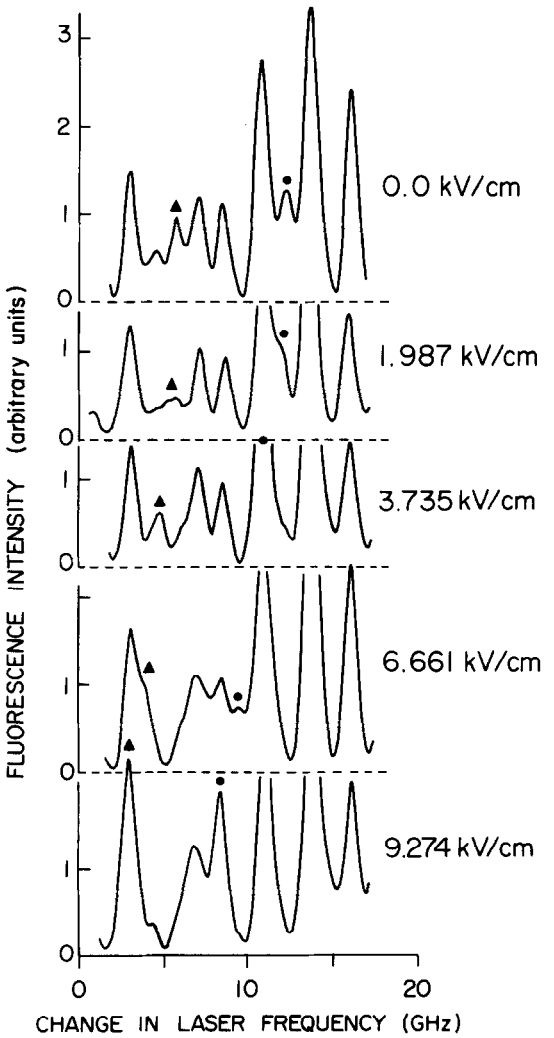

FIG. 3. Variation with electric field of the HSO lines near 16 472 cm^{-1}, recorded in perpendicular polarization. Circles mark the movement of the F_1 0_{00}–1_{10} line, and triangles that of the F_2 0_{00}–1_{10} line. The vertical displacement of the spectra is linear in the applied electric field.

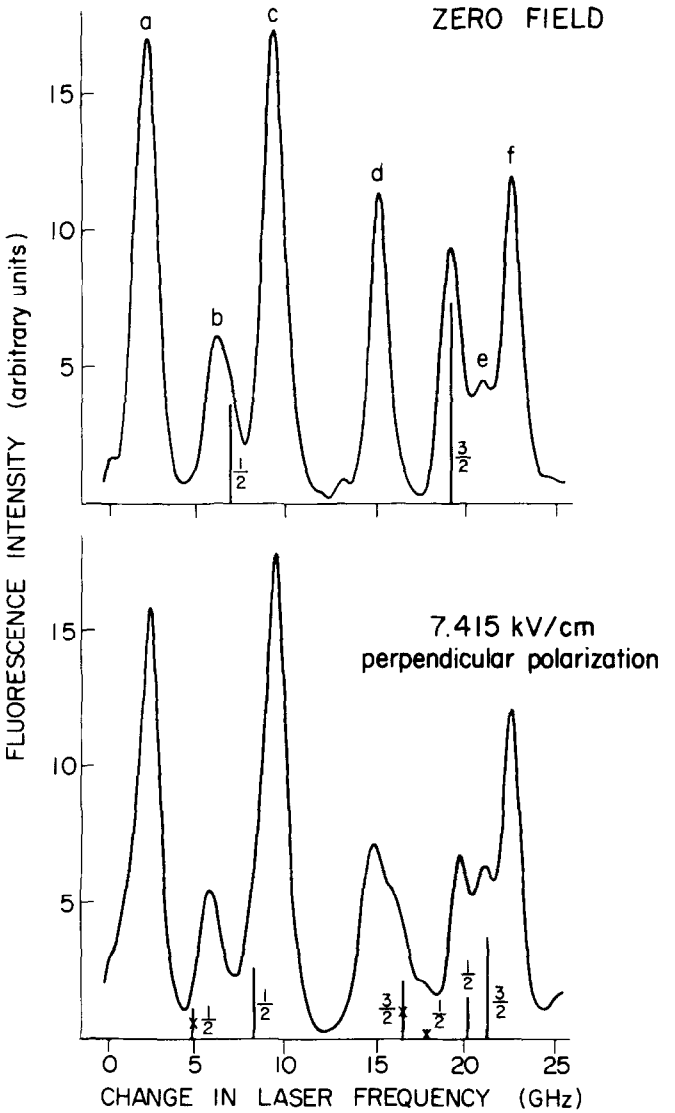

FIG. 4. The high-resolution fluorescence excitation spectrum of HSO near 16 493 cm^{-1}, recorded at zero-field and at 7.415 kV/cm in perpendicular polarization. In the zero-field spectrum lines a, c, d, and f are assigned to the F_1 $11_{1,10}$–$10_{0,10}$, F_1 $17_{3,14}$–$17_{2,16}$, F_1 $12_{3,10}$–$13_{2,12}$, and F_2 $11_{2,10}$–$11_{1,10}$ lines, respectively. Also shown as a stick spectrum are the relative intensities and positions, identified by J', of the spin components of the 1_{10}–0_{00} transition. In the high-field spectrum a stick spectrum gives the relative intensities and positions, denoted by $|M'_J|$, calculated for μ''_a = 2.20 D and μ'_a = 1.05 D at the applied field. An "X" marks a transition forbidden at zero field.

The Stark shifts of the analogous 1_{10}–0_{00} transitions are presented in Figs. 4 and 5 for perpendicular and parallel polarizations, as indicated. Again the zero-field 1_{10}–0_{00} lines at 16 493.022 and 16 493.449 cm^{-1} are identified from the published

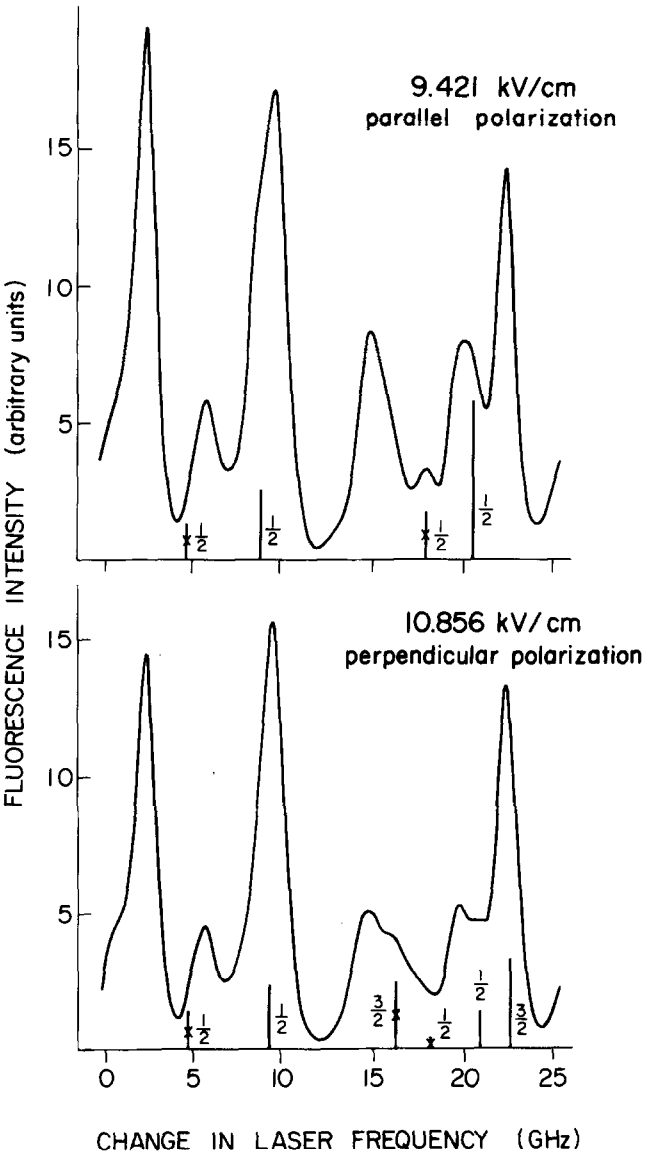

FIG. 5. The same spectrum as that in Fig. 4, with a field of 9.421 kV/cm in parallel polarization, and 10.856 kV/cm in perpendicular polarization.

line listings (*3*). As the electric field increases the 1_{10}–0_{00} lines lose intensity and tune to higher frequency. In addition, new lines appear to the lower-frequency side of the zero-field line positions. These lines belong to the 1_{11}–0_{00} transitions which gain intensity in the presence of an electric field. To understand the observed Stark shifts shown in Figs. 3–5 it is necessary to review briefly the Stark effect in a doublet electronic state of an asymmetric top.

4. THE STARK EFFECT IN HSO

HSO is an asymmetric top very close to the prolate limit ($\kappa \simeq -0.99$) in both its ground and excited electronic state. The angular momenta **N** (molecular rotation), **S** (electron spin), and **I** (nuclear spin) couple according to Hund's case ($b_{\beta J}$) (*9*)

$$\mathbf{N} + \mathbf{S} = \mathbf{J}, \qquad \mathbf{J} + \mathbf{I} = \mathbf{F}. \tag{1}$$

The interactions involving $^1H(I = 1/2)$, are too small to produce hyperfine structure resolvable in the Doppler-limited studies reported here, and we consider only **N**, **S**, and **J**. All levels with $N > 0$ are split into doublets for which J takes the values $J = N + (1/2)$ (F_1) and $J = N - (1/2)$ (F_2). In the case where $N = 0$, $J = 1/2$ only.

The electric dipole moment of HSO has components along the a and b inertial axes of this planar molecule. In an electric field, the rotational energy levels can be represented by a Hamiltonian comprising terms for the rigid-rotor energy, centrifugal distortion, spin–rotation, and the Stark effect. Since the rotational line assignments and molecular constants are known (*3*) for the $\tilde{A}(003)$–$\tilde{X}(000)$ band, we need only consider the Stark Hamiltonian, H_S, to calculate the lineshifts with applied electric field, E_Z:

$$H_S = -\boldsymbol{\mu} \cdot \mathbf{E} = -E_Z \sum_{g=a,b} \mu_g \Phi_{Zg}, \tag{2}$$

where Z is the field direction in a laboratory-fixed coordinate system, μ_g are components of the dipole moment along the principal inertial axes a and b, and Φ_{Zg} represents the projections (direction cosines) of the molecular axes onto the field direction Z. The matrix elements of H_S given by Bowater *et al.* (*10*) and by Landsberg *et al.* (*11*) may be rewritten using a basis set chosen so that the asymmetric-top levels are represented by Wang combinations of symmetric-top wavefunctions, i.e.,

$$|NKpJM_J\rangle = \frac{1}{2^{1/2}}\{|NKJM_J\rangle + p|N\text{-}KJM_J\rangle\} \tag{3}$$

for $K \neq 0$. Here $p = 1$ (+parity level) or -1 (−parity level), and K refers to the component of the total angular momentum about the top axis in the prolate limit (i.e., K_a or K_{-1}). For $K = 0$, then $|NKpJM_J\rangle$ becomes simply $|NOJM_J\rangle$.

The matrix elements of H_S are then given by

$$\langle N'K'p'J'M_J|-\mu_Z E_Z|NKpJM_J\rangle = \frac{Q}{2}(-1)^{K'}(R\mu_a + S\mu_b)E_Z, \tag{4}$$

where

$$R = [1 - pp'(-1)^{N+N'}]\begin{pmatrix} N & N' & 1 \\ K & -K' & 0 \end{pmatrix}, \tag{5}$$

$$S = \frac{1}{2^{1/2}}[1 + pp'(-1)^{N+N'}]\left[\begin{pmatrix} N & N' & 1 \\ K & -K' & -1 \end{pmatrix} - \begin{pmatrix} N & N' & 1 \\ K & -K' & 1 \end{pmatrix}\right], \tag{6}$$

and

$$Q = (-1)^{J'+J-M-1/2}[(2N+1)(2N'+1)(2J+1)(2J'+1)]^{1/2} \times \begin{pmatrix} J & J' & 1 \\ M & -M & 0 \end{pmatrix} \begin{Bmatrix} 1 & N & N' \\ 1/2 & J' & J \end{Bmatrix}. \quad (7)$$

Equation (4) applies to all cases except when either (but not both) K' or K is zero; then the result must be multiplied by the factor $2^{1/2}$.

The Stark Hamiltonian has matrix elements connecting states with $\Delta N = 0$, ± 1 and $\Delta J = 0$, ± 1. States with $\Delta K = 0$, and $\Delta K = \pm 1$, are connected through μ_a, and μ_b, respectively. For HSO, the largest Stark shifts are produced by interaction between levels of the same K with small asymmetry doubling, or accidentally near-degenerate levels with $\Delta K = \pm 1$.

In this study, the Stark effect is measured only for transitions of the type $N = 0$, $K = 0$ (0_0) $\leftrightarrow$ $N = 1$, $K = 1$ (1_1) in the symmetric-top limit. Furthermore, because the 0_0–1_1 energy separation within either electronic state is large ($A'' + B'' \simeq 320$ GHz, $A' + B' \simeq 309$ GHz) compared with the 0_0–1_0 energy separation ($2B'' \simeq 41$ GHz, $2B' \simeq 34$ GHz) the Stark effect calculation is greatly simplified. We make the approximation that the $0_{00}(J = 1/2, |M_J| = 1/2)$ levels shift with the square of the applied field only through their interaction with the higher energy $1_{01}(J = 3/2, |M_J| = 1/2)$ and $1_{01}(J = 1/2, |M_J| = 1/2)$ levels. Therefore only these levels are used in calculating the shift by diagonalizing the appropriate Stark matrix.

The 1_1 asymmetry splittings (*3, 12*) of 1.36 GHz (ground state) and 1.14 GHz (excited state) combine with the spin–rotation splittings (*3*) of 8.15 GHz (ground state) and 12.8 GHz (excited state) to produce two nearby pairs of levels. In an electric field the $|M_J|$ values result in six levels, four of which have $|M_J| = 1/2$ and two with $|M_J| = 3/2$. Because the contribution from matrix elements connecting states with $\Delta K_a = \pm 1$ is considered negligible in this case, only terms involving the

TABLE I

Stark Hamiltonian Matrix Elements for $N = K_a = 1$

$\lvert J \lvert M_J\rvert, p\rangle$	$\lvert\frac{3}{2}\frac{1}{2},-1\rangle$	$\lvert\frac{3}{2}\frac{1}{2},1\rangle$	$\lvert\frac{1}{2}\frac{1}{2},-1\rangle$	$\lvert\frac{1}{2}\frac{1}{2},1\rangle$	$\lvert\frac{3}{2}\frac{3}{2},-1\rangle$	$\lvert\frac{3}{2}\frac{3}{2},1\rangle$
	D_1	$-\frac{1}{6}\mu_a E_Z$	0	$-\frac{\sqrt{2}}{6}\mu_a E_Z$		
		D_2	$-\frac{\sqrt{2}}{6}\mu_a E_Z$	0		
			D_3	$-\frac{1}{3}\mu_a E_Z$		
				D_4		
					D_5	$-\frac{1}{2}\mu_a E_Z$
						D_6

The D_i are the field-independent energies of the ith levels; $D_1 = D_5$ and $D_2 = D_6$.

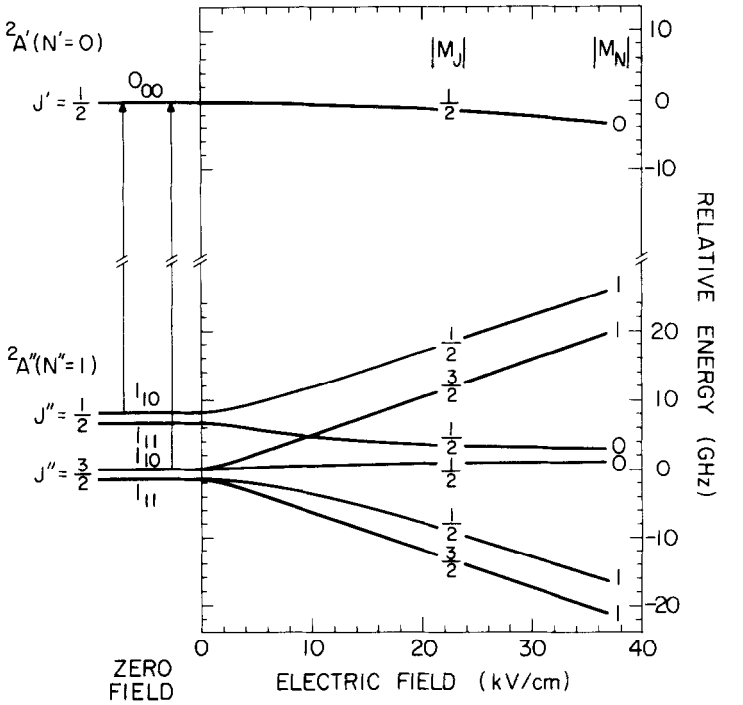

FIG. 6. The Stark effect for the levels of the 0_{00}–1_{10} and 0_{00}–1_{11} transitions, using $\mu_a'' = 2.20$ D and $\mu_a' = 1.05$ D.

μ_a component of the dipole moment are included. Substituting $N = 1$ and $K = 1$ in the Stark Hamiltonian, we see that for the interaction among the four $|M_J| = 1/2$ levels, the problem reduces to the diagonalization of a 4×4 symmetric matrix. For the interaction between the two $|M_J| = 3/2$ levels, only a 2×2 matrix needs to be diagonalized. The elements of these matrices are given in Table I; their diagonalization yields the eigenvalues, which determine the Stark shifts, and the eigenvectors, which determine the relative intensities of the lines. When the $\Delta M_J = 0$ transitions are selected (polarization parallel to the field), and the zero-field intensities chosen, the eigenvectors of the 4×4 matrix give the relative intensities directly. However, for the six possible $\Delta M_J = \pm 1$ transitions (polarization perpendicular to the field), the $|M_J| = 3/2$ levels must also be considered. The intensities of the $|M_J| = 3/2 \leftrightarrow 1/2$ transitions relative to the $|M_J| = 1/2 \leftrightarrow 1/2$ transitions are three times greater at zero-field, as found by application of the Wigner–Eckart theorem.

The shifts of energy levels associated with the F_1 and F_2 components of the 0_{00}–1_{10} transitions are shown in Fig. 6 for electric fields up to 40 kV/cm and using $\mu_a'' = 2.20$ D and $\mu_a' = 1.05$ D. At zero-field, only these two transitions are possible, having relative intensities 1 and 2, respectively. In an electric field levels of opposite parity mix, causing the appearance of transitions forbidden at zero-field. As the electric field increases, the 1_{11} levels take on more 1_{10} character to give increasing intensity to the 0_{00}–1_{11} transitions at the expense of the 0_{00}–1_{10} transitions. In the

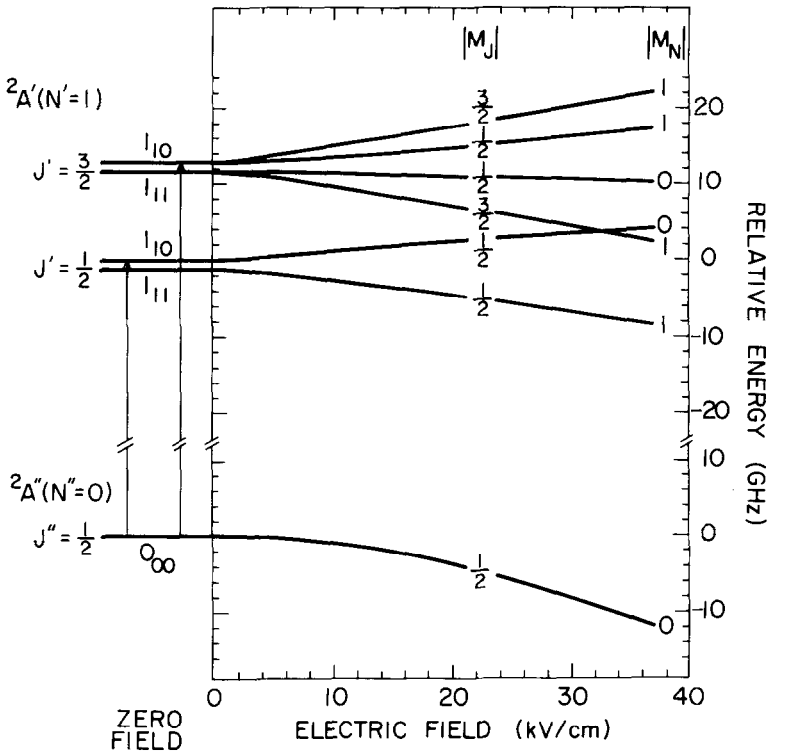

FIG. 7. The Stark effect for the levels of the 1_{10}–0_{00} and 1_{11}–0_{00} transitions, using $\mu_a'' = 2.20$ D and $\mu_a' = 1.05$ D.

high-field limit, both transitions have equal intensity. A magnetic field removes the $2J + 1$ degeneracy of the M_J levels, whereas an electric field leaves each level doubly degenerate (except for $M_J = 0$) since levels of $+M_J$ and $-M_J$ have the same Stark energy. Consequently, both parallel ($\Delta M_J = 0$) and perpendicular ($\Delta M_J = \pm 1$) polarization can connect, for example, two $|M_J| = 1/2$ levels.

In the limit of small asymmetry splittings, the first-order Stark effect in doublet electronic states may be written for each $J = N \pm 1/2$ component:

$$\langle NKpJM_J|\mu_Z E_Z|NKpJM_J\rangle = \pm \frac{\mu_a E_Z |M_J| K}{(N + 1/2)(J + 1/2)}. \tag{8}$$

Landsberg *et al.* (*11*) have discussed the high-field limit

$$\langle NKpJM_J|\mu_Z E_Z|NKpJM_J\rangle = \pm \frac{\mu_a E_Z |(M_J \pm 1/2)| K}{N(N + 1)}, \tag{9}$$

when $M_N = M_J \pm 1/2$ becomes the good quantum number and an electric field analog of the Paschen–Back effect is seen. The $|M_N|$ values in the high-field limit are indicated in Figs. 6 and 7.

Figure 7 shows the shifts of the energy levels associated with the F_1 and F_2 components of the 1_{10}–0_{00} transitions, again using $\mu_a'' = 2.20$ D and $\mu_a' = 1.05$ D.

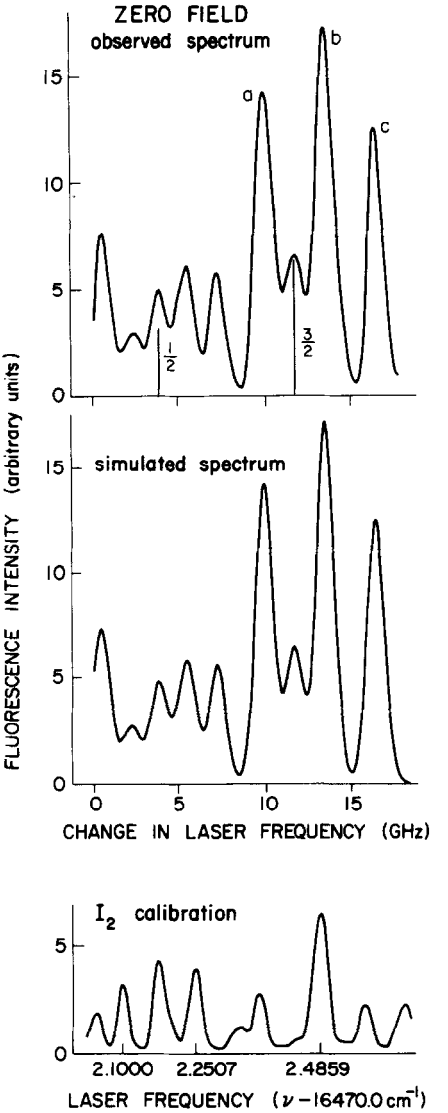

FIG. 8. The high-resolution fluorescence excitation spectrum near 16 472 cm^{-1} with the simulated spectrum and I_2 calibration spectrum. The calculated relative intensities and line positions, identified by J'', of the 0_{00}–1_{10} F_1 and F_2 components are indicated. Features a, b, and c are assigned by Ref. (*3*) to the F_2 3_{03}–3_{13}, F_1 3_{03}–3_{13}, and F_2 $23_{2,21}$–$22_{1,21}$ lines, respectively.

These transitions are simply the inverse of those shown in Fig. 6, except that the $J = N \pm 1/2$ separation is larger, the asymmetry doubling smaller, and the energy level ordering different because of the measured (*3*) signs of the spin–rotation interaction constants ϵ'_{aa} (+) and ϵ''_{aa} (−). In addition, the difference between the electronic state dipole moments means that lineshifts of the 1_{10}–0_{00} and 1_{11}–0_{00} transitions will contain a larger contribution from the 0_{00} level shift than those of

the 0_{00}–1_{10} and 0_{00}–1_{11}. Hence the latter transitions will shift predominantly due to μ_a'', while the former will shift according to μ_a' and μ_a''.

5. DETERMINATION OF THE DIPOLE MOMENTS

To find the ground-state dipole moment, the zero-field spectrum is simulated by adjusting the widths, intensities, and positions of all lines in the region studied. Then the Stark-shifted spectrum is generated by using the eigenvalues and eigenvectors of the Stark Hamiltonian containing only one adjustable parameter, namely, the ground-state dipole moment. The excited-state dipole moment, which affects the small second-order shift of the 0_{00} level (see Fig. 6), is fixed. Once an accurate value of the ground-state dipole moment is determined, then the excited-state dipole moment is found by selected simulation of the analogous Stark shifts for the excited state. This process is iterated until a convergent best fit is obtained. The quality of the fit is judged only by visual inspection.

We discuss first the determination of the ground-state dipole moment by analysis of the Stark effect on the 0_{00}–1_{10} and 0_{00}–1_{11} lines near 16 472 cm^{-1} (see Fig. 3). Figure 8 compares the simulated and observed zero-field spectra. Gaussian linewidths of 1.2 GHz (FWHM) are required for the simulation, slightly larger than the room-temperature Doppler width (0.9 GHz).

Figures 9 and 10 compare the observed and simulated spectra for applied fields of 6.661 and 9.274 kV/cm, respectively. For the 6.661-kV/cm simulation, the $0_{00}(J = 1/2, |M_J| = 1/2) - 1_{10}(J = 3/2, |M_J| = 3/2)$ line is clearly visible, enabling a very accurate determination of the lineshift to be made. The shoulder which remains midway between the two components of the low J transition is an unassigned line whose presence at zero-field serves to increase the apparent intensity of this transition. The dye laser frequency is then fixed to excite the neighboring low-frequency line and the field increased until a maximum fluorescence signal is seen. This occurs at a field of 9.274 kV/cm, where the $0_{00}(J = 1/2, |M_J| = 1/2)$–$1_{10}(J = 3/2, |M_J| = 3/2)$ and $0_{00}(J = 1/2, |M_J| = 1/2)$–$1_{11}(J = 1/2, |M_J| = 1/2)$ transitions virtually coincide, as shown in Fig. 10. Even at these moderately high fields, other lines show very little field effects. The lines labeled *a* and *b* in Fig. 8 are assigned by Kakimoto *et al.* (*3*) to the F_1 and F_2 components of the 3_{03}–3_{13} line at 16 472.500 and 16 472.390 cm^{-1}, respectively. These lines are expected to broaden slightly and show small second-order shifts to higher frequency as the electric field is increased. This is observed experimentally, and included in the simulation program, although even for the highest field used (9.274 kV/cm) the shift amounts to only $\simeq$0.25 GHz. Line c is assigned (*3*) to the F_2 component of the $23_{2,21}$–$22_{1,21}$ line at 16 472.589 cm^{-1}, and all other lines are not identified. The electric field spectra, however, show no apparent Stark effect for these lines, which we therefore conclude are high J lines.

The ground-state dipole moment is determined from the six values of the applied electric field shown in Fig. 3. Numerous intermediate fields are recorded as supporting data. We find

$$\mu_a'' = 2.20 \pm 0.08 \text{ D} \tag{10}$$

in the $\tilde{X}(000)$ state using the final value of μ_a'. Table II lists the calculated lineshifts

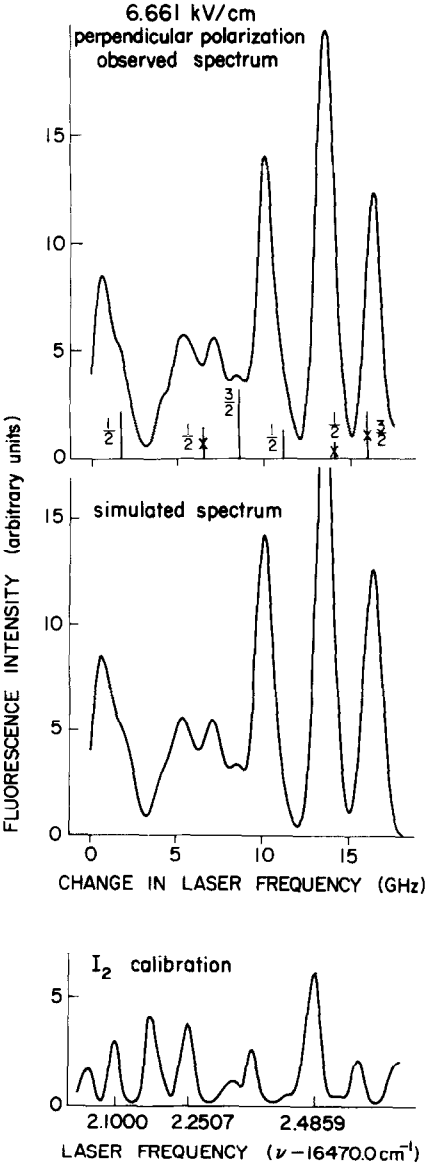

FIG. 9. The same spectral region as that in Fig. 8, recorded in perpendicular polarization with a field of 6.661 kV/cm across the plates. The relative frequencies and intensities of the six $|M_J''|$ components of the 0_{00}–1_{10} and 0_{00}–1_{11} lines are given, using $\mu_a'' = 2.20$ D and $\mu_a' = 1.05$ D.

and relative intensities of the $|M_J|$ components which correlate to the 0_{00}–1_{10} and 0_{00}–1_{11} transitions. Thus lineshifts of nearly 5 GHz are possible at the highest field (9.274 kV/cm) used.

The excited-state dipole moment is determined from the Stark effect on the 1_{10}–0_{00} and 1_{11}–0_{00} lines. Figures 4 and 5 illustrate the observed spectra in the relevant

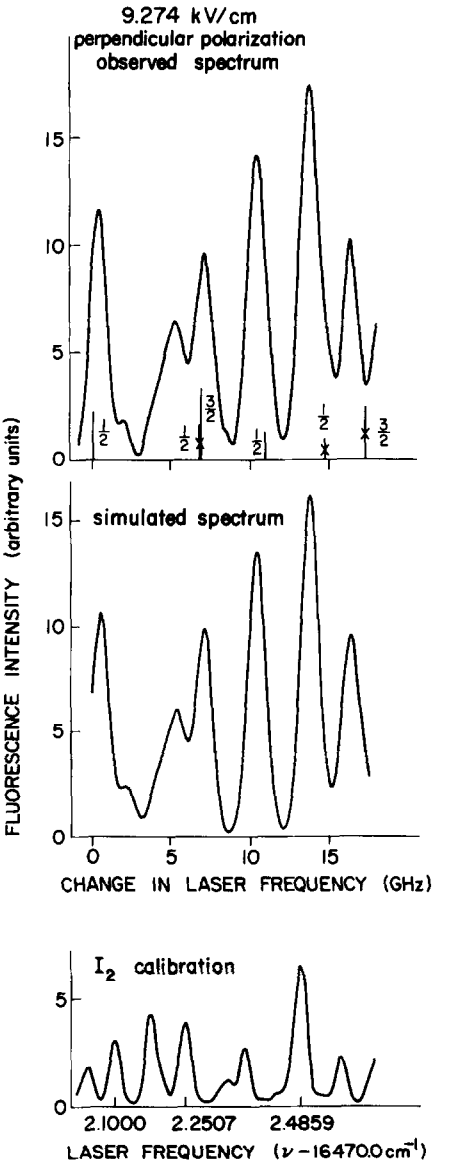

FIG. 10. The same spectral region as that in Fig. 8, with a field of 9.274 kV/cm, in perpendicular polarization.

spectral region for applied fields up to 10.856 kV/cm. These spectra show that the 1_{10}–0_{00} lines are each blended to some extent: the $J = 1/2$ line (F_2 component) by a lower-frequency unassigned line which shows no Stark effect, and the $J = 3/2$ line (F_1 component) by a weaker line which is also unassigned and shows no Stark effect. Lines a, c, d, and f are all assigned (3) to high J ($J \geq 10\frac{1}{2}$) transitions while lines b and e are unidentified. Lines c and d, however, couple levels of K_a

TABLE II

Lineshifts (GHz) and Relative Intensities in Parentheses as a Function of Applied Electric Field

Lower Level of Transition $0_{00}(J'=1/2, \lvert M_J'\rvert=1/2)$ – $1_{K_aK_c}(J'', \lvert M_J''\rvert)$	Electric Field (kV/cm)					
	0.0	1.987	3.735	5.575	6.661	9.274
$1_{10}(1/2,1/2)$	0.0 (0.33)	-0.363 (0.28)	-0.996 (0.24)	-1.791 (0.21)	-2.297 (0.20)	-3.599 (0.19)
$1_{11}(1/2,1/2)$	0.0 (0.0)	0.268 (0.05)	0.683 (0.10)	1.096 (0.12)	1.311 (0.13)	1.722 (0.14)
$1_{10}(3/2,3/2)$	0.0 (0.50)	-0.627 (0.38)	-1.535 (0.33)	-2.566 (0.30)	-3.191 (0.29)	-4.734 (0.28)
$1_{10}(3/2,1/2)$	0.0 (0.17)	-0.068 (0.16)	-0.200 (0.14)	-0.377 (0.12)	-0.487 (0.11)	-0.764 (0.10)
$1_{11}(3/2,1/2)$	0.0 (0.0)	0.109 (0.01)	0.363 (0.03)	0.733 (0.04)	0.991 (0.05)	1.704 (0.07)
$1_{11}(3/2,3/2)$	0.0 (0.0)	0.600 (0.12)	1.460 (0.17)	2.396 (0.20)	2.950 (0.20)	4.266 (0.22)

= 2 and 3 which have very small asymmetry splittings and therefore a linear dependence of their shift with electric field. Although the high J values do not allow the lines to tune fast with applied electric field, their intensity and line position changes are not negligible and prevent a full simulation of the Stark spectra using a single adjustable parameter.

In Figs. 4 and 5 only the observed spectra are shown. The line positions and their relative intensities, calculated using dipole moments of $\mu_a' = 1.05$ D and $\mu_a'' = 2.20$ D, are indicated in a stick spectrum for the lines belonging to the 1_{10}–0_{00} and 1_{11}–0_{00} transitions. At 7.415 kV/cm both $|M_J|$ components correlating in zero-field to the forbidden $F_1 1_{11}$–0_{00} transition are clearly identified (see Fig. 4). The highest field studied, 10.856 kV/cm, is the field required to superimpose the $1_{10}(J = 3/2, |M_J| = 3/2)$–$0_{00}(J = 1/2, |M_J| = 1/2)$ component and the F_2 component of the $11_{2,10}$–$11_{1,10}$ line.

The value of the $\tilde{A}(003)$ dipole moment along the a axis is determined to be

$$\mu_a' = 1.05 \pm 0.08 \text{ D} \tag{11}$$

when the final value of μ_a'' is used in the analysis.

The principal uncertainty in these dipole moments reflects the accuracy to which the Stark shifts can be measured. The percentage error in the excited-state dipole moment is about twice that in the ground state for two reasons. First, the ground-state dipole moment contributes more significantly to the Stark shifts used to determine the excited-state dipole moment than the converse. Second, these shifts are less accurately measured because of the Stark shift of neighboring features.

6. DISCUSSION

Our knowledge of the dipole moments for the ground states of small polyatomic molecules is extensive, as a result of infrared, microwave, and molecular beam electric resonance studies (*13*). In contrast, there are very few determinations of excited state dipole moments. Examples are the $\tilde{A}$ and $\tilde{a}$ states of H_2CO (*14–17*), and the $\tilde{A}$ states of HC_2CHO (*18*), HFCO (*19*), H_2CS (*20*), NHD (*21*), and HNO (*22*). The present study is similar to that of Freeman and Klemperer (*14*) in that Doppler-limited dc Stark shifts are observed and analyzed. Whereas Freeman and Klemperer used a white light source and recorded the Stark spectrum in absorption with a 10-m spectrograph, the present study on HSO utilizes a narrow-band tunable laser to record the Stark spectrum in undispersed fluorescence.

The major interest in electric dipole moments is the understanding they provide of the bonding and charge distribution in the state of interest. In the course of this study both the $\tilde{A}$- and $\tilde{X}$-state dipole moments of HSO were measured to an accuracy of 4 and 8%, respectively. It should be possible to improve these dipole moment determinations by a variety of techniques, but the accuracy of the present measurements are sufficient to permit a quantitative comparison with ab initio electronic structure calculations.

Traditionally, chemists have crudely estimated ground-state dipole moments by vectorially combining the moments of molecular groups. The HSO angle is experimentally determined to be 106.6° and 95.7° in the $\tilde{X}$ and $\tilde{A}$ states, respectively (*3, 23*). The *a* axis lies virtually along the S–O bond in both states. We take the μ_{SO} and μ_{HS} group dipole moments to be 1.65 and 0.70 D from the measured dipole moments and known geometries of H_2S and SO_2. Because the O atom is more electronegative than the S atom, which in turn is more electronegative than the H atom, the *a* components of μ_{SO} and μ_{HS} point in the same direction, yielding a value of 1.8 D for μ_a''. This estimate is 20% lower than what we measure, but immediately suggests that the ground-state dipole moment of HSO should be sizable.

TABLE III

Comparison between Experimental and Theoretical Values of the Dipole Moments for HSO and HO_2

Molecule	State	Experiment			Theory	
		Region	μ_a(D)	μ_{total}(D)	μ_a(D)	μ_{total}(D)
HSO	$\tilde{X}^2A''$	Optical	2.20±0.08 [a]	–	2.067 [b]	2.274 [b], 2.1 [c], 2.4 [c]
	$\tilde{A}^2A'$	Optical	1.05±0.08 [a]	–	1.25 [b]	1.785 [b]
HO_2	$\tilde{X}^2A''$	Microwave	1.412±0.033 [d]	2.090±0.034 [d]	1.207 [e]	2.295 [e], 2.11 [c], 2.33 [c]
	$\tilde{A}^2A'$	–	–	–	0.916 [e]	2.138 [e]

[a]this work; [b]reference (5); [c]reference (6); [d]reference (27); [e]reference (26).

The HSO $\tilde{A}$–$\tilde{X}$ system is an n to π^* transition whose weak intensity is consistent with the experimentally determined $\tilde{A}$-state lifetime of about 40 μsec (*24*). Here, an electron in a nonbonding orbital in the molecular plane localized on the oxygen atom jumps to an antibonding orbital perpendicular to the molecular plane delocalized over the S–O bond. Consequently, charge is transferred from O to S, and the excited-state dipole moment is expected to decrease from its ground-state value. While this prediction is borne out by our experiment, it is well known that simple molecular orbital theory cannot provide quantitative values of dipole moments (*25*).

Table III compares the experimentally determined dipole moments of HSO with the SCF CI calculations of Sannigrahi *et al.* (*5*) and Hinchliffe (*6*). It is important to recognize that the theoretical values refer to the equilibrium geometries of the $\tilde{A}$ and $\tilde{X}$ states while the experimental values refer to the (003) and (000) levels of these states, respectively. The agreement is judged to be excellent. Also shown in Table III is the corresponding comparison for HO_2, the isovalent analog of HSO. Once again configuration interaction calculations (*6, 26*) are able to match the experimentally determined dipole moment (*27*) within a few tenths of a debye. As pointed out by Sannigrahi *et al.* (*5*), the interpretation of the change in the dipole moment between the HSO $\tilde{X}$ and $\tilde{A}$ states is rather subtle and cannot be attributed to a change in the occupancies of the n and π^* molecular orbitals alone. Nevertheless, the agreement between theory and experiment is very heartening because it tells us that, at least with regard to the dipole moments, the major features of the electronic structure of these light triatomic molecules are understood.

ACKNOWLEDGMENTS

The authors would like to thank Chris A. Greene for much help and advice concerning the calculation of the Stark effect in HSO. We also thank George C. Kottler who fabricated the precision Stark spacers. Support from the National Science Foundation under Grant NSF CHE 80-06524 is gratefully acknowledged.

RECEIVED: September 29, 1981

REFERENCES

1. K. H. BECKER, M. A. INOCÊNCIO, AND U. SCHURATH, *Int. J. Chem. Kinet. Symp.* **1,** 205–220 (1975).
2. U. SCHURATH, M. WEBER, AND K. H. BECKER, *J. Chem. Phys.* **67,** 110–119 (1977).
3. M. KAKIMOTO, S. SAITO, AND E. HIROTA, *J. Mol. Spectrosc.* **80,** 334–350 (1980).
4. Y. ENDO, S. SAITO, AND E. HIROTA, *J. Chem. Phys.* **75,** 4379–4384 (1981).
5. A. B. SANNIGRAHI, K. H. THUNEMANN, S. D. PEYERIMHOFF, AND R. J. BUENKER, *Chem. Phys.* **20,** 25–33 (1977).
6. A. HINCHLIFFE, *J. Mol. Struct.* **66,** 235–242 (1980).
7. F. C. FEHSENFELD, K. M. EVENSON, AND H. P. BROIDA, *Rev. Sci. Instrum.* **36,** 294–298 (1965).
8. S. GERSTENKORN AND P. LUC, "Atlas du spectre d'absorption de la molécule d'iode," Ed. du CNRS, Paris, 1978.
9. C. H. TOWNES AND A. L. SCHAWLOW, "Microwave Spectroscopy," Dover, New York, 1975.
10. I. C. BOWATER, J. M. BROWN, AND A. CARRINGTON, *Proc. R. Soc. Ser. A* **333,** 265–288 (1973).
11. B. M. LANDSBERG, A. J. MERER, AND T. OKA, *J. Mol. Spectrosc.* **67,** 459–475 (1977).
12. S. R. POLO, *Canad. J. Phys.* **35,** 880–885 (1957).

13. W. GORDY AND R. L. COOK, "Microwave Molecular Spectra," Wiley, New York, 1970; A. L. MCCLELLAN, "Tables of Experimental Dipole Moments," Freeman, San Francisco, 1963; R. D. NELSON, D. R. LIDE, JR., AND A. A. MARYOTT, "Selected Values of Electric Dipole Moments for Molecules in the Gas Phase," U. S. National Bureau of Standards NSRDS-NBS10, U. S. Government Printing Office, Washington, D. C., 1967.
14. D. E. FREEMAN AND W. KLEMPERER, *J. Chem. Phys.* **40,** 604–605 (1963); D. E. FREEMAN AND W. KLEMPERER, *J. Chem. Phys.* **45,** 52–57 (1966).
15. J. R. LOMBARDI, D. E. FREEMAN, AND W. KLEMPERER, *J. Chem. Phys.* **46,** 2746–2749 (1967).
16. N. J. BRIDGE, D. A. HANER, AND D. A. DOWS, *J. Chem. Phys.* **48,** 4196–4210 (1967).
17. A. D. BUCKINGHAM, D. A. RAMSAY, AND J. TYRELL, *Canad. J. Phys.* **48,** 1242–1253 (1969).
18. D. E. FREEMAN, J. R. LOMBARDI, AND W. KLEMPERER, *J. Chem. Phys.* **45,** 58–60 (1966).
19. J. R. LOMBARDI, D. CAMPBELL, AND W. KLEMPERER, *J. Chem. Phys.* **46,** 3482–3486 (1967).
20. R. N. DIXON AND C. R. WEBSTER, *J. Mol. Spectrosc.* **70,** 314–322 (1978).
21. J. M. BROWN, S. W. CHALKLEY, AND F. D. WAYNE, *Mol. Phys.* **38,** 1521–1537 (1979).
22. R. N. DIXON AND M. NOBLE, *Chem. Phys.* **50,** 331–339 (1980).
23. N. OHASHI, M. KAKIMOTO, S. SAITO, AND E. HIROTA, *J. Mol. Spectrosc.* **84,** 204–224 (1980).
24. M. KAWASAKI, private communication. See also M. Kawasaki, K. Kasakani and H. Sato, *Chem. Phys. Lett.* **75,** 128–131 (1980).
25. S. GREEN, *Advan. Chem. Phys.* **25,** 179–209 (1974).
26. R. J. BUENKER AND S. D. PEYERIMHOFF, *Chem. Phys. Lett.* **37,** 208–211 (1976).
27. S. SAITO AND C. MATSUMURA, *J. Mol. Spectrosc.* **80,** 34–40 (1980).